Atmospheric rivers increase future flood risk in western Canada's largest Pacific river

Charles L. Curry, Siraj ul Islam, Francis W. Zwiers, & Stephen J. Déry

2019

Original citation:

Curry, C. L., Islam, S. ul, Zwiers, F. W., & Déry, S. J. (2019). Atmospheric rivers increase future flood risk in western Canada's largest Pacific river. *Geophysical Research Letters*, *46*(3), 1651–1661. https://doi.org/10.1029/2018GL080720

AGU100 ADVANCING EARTH AND SPACE SCIENCE

Geophysical Research Letters

RESEARCH LETTER
10.1029/2018GL080720

Special Section:
Atmospheric Rivers: Intersection of Weather and Climate

Atmospheric Rivers Increase Future Flood Risk in Western Canada's Largest Pacific River

C. L. Curry[1,2], S. U. Islam[3], F. W. Zwiers[1], and S. J. Déry[3]

[1]Pacific Climate Impacts Consortium, University of Victoria, Victoria, British Columbia, Canada, [2]School of Earth and Ocean Sciences, University of Victoria, Victoria, British Columbia, Canada, [3]Environmental Science and Engineering Program, University of Northern British Columbia, Prince George, British Columbia, Canada

Key Points:
- The Fraser River Basin transitions from a 100% snowmelt freshet to a 25% rainfall peak flow regime by the 2080s under the RCP8.5 scenario
- Increasing influence of atmospheric rivers prompts a quadrupling of cold season extreme rainfall frequency in the basin from 1990s to 2080s
- Hydrologic modeling indicates peak streamflow events of historic proportions, and of unprecedented frequency, by the late 21st century

Supporting Information:
- Supporting Information S1

Correspondence to:
C. L. Curry,
cc@uvic.ca

Citation:
Curry, C. L., Islam, S. U., Zwiers, F. W., & Déry, S. J. (2019). Atmospheric rivers increase future flood risk in Western Canada's largest Pacific River. *Geophysical Research Letters*, *46*, 1651–1661. https://doi.org/10.1029/2018GL080720

Received 30 SEP 2018
Accepted 16 JAN 2019
Accepted article online 22 JAN 2019
Published online 6 FEB 2019

Abstract Snow-dominated watersheds are bellwethers of climate change. Hydroclimate projections in such basins often find reductions in annual peak runoff due to decreased snowpack under global warming. British Columbia's Fraser River Basin (FRB) is a large, nival basin with exposure to moisture-laden atmospheric rivers originating in the Pacific Ocean. Landfalling atmospheric rivers over the region in winter are projected to increase in both strength and frequency in Coupled Model Intercomparison Project Phase 5 climate models. We investigate future changes in hydrology and annual peak daily streamflow in the FRB using a hydrologic model driven by a bias-corrected Coupled Model Intercomparison Project Phase 5 ensemble. Under Representative Concentration Pathway (8.5), the FRB evolves toward a nival-pluvial regime featuring an increasing association of extreme rainfall with annual peak daily flow, a doubling in cold season peak discharge, and a decrease in the return period of the largest historical flow, from a 1-in-200-year to 1-in-50-year event by the late 21st century.

Plain Language Summary Snow-covered areas of the globe are particularly sensitive to global warming. Future projections using global climate models generally show that as the ratio of snow to rain declines, river flows peak earlier in the year with reduced volume. These models also capture the phenomenon of "atmospheric rivers": long, meandering plumes of water vapor often originating over the tropical oceans that bring sustained, heavy precipitation to the west coasts of North America and northern Europe. The present-day frequency of landfalling atmospheric rivers on the Canadian west coast is projected to increase nearly fourfold by the late 21st century, with a proportionate increase in extreme rainfall events. Our work is the first to directly investigate the impact of these "rivers in the sky" on "rivers on the land" using climate model projections. Focusing on the Fraser River Basin, Canada's largest Pacific watershed, and using a business-as-usual industrial emissions scenario, we show that the basin transitions from one where peak flow results from spring snowmelt to one where peak flow is often caused by extreme rainfall. Our modeling suggests that extreme rainfall events resulting from atmospheric rivers may lead to peak annual floods of historic proportions, and of unprecedented frequency, by the late 21st century in the Fraser River Basin.

1. Introduction

An intensification of Earth's hydrologic cycle is projected in most global climate model (GCM) simulations comprising the Coupled Model Intercomparison Project Phase 5 (CMIP5; Taylor et al., 2012). For example, rising surface air temperature over the next century prompts robust increases in precipitation and evaporation over the oceans (Collins & Knutti, 2013). Regionally, projections are somewhat less robust; but over land areas having net positive annual runoff, an intensification of existing precipitation patterns is projected (Roderick et al., 2014). Precipitation increases are a particular concern for large hydrologic basins, insofar as their integrated effect could increase flood risk (Kundzewicz et al., 2007; Milly et al., 2002). In nival basins relatively isolated from maritime moisture sources, however, freshet flows simulated in hydrologic models driven by GCMs usually decrease in future (Hanzer et al., 2018). Under projected warming, the snow-to-rain ratio and spring snowpack dwindle (Krasting et al., 2013; Pierce & Cayan, 2013), shifting the freshet earlier and reducing its peak magnitude.

The Fraser River Basin (FRB) of British Columbia (BC), Canada's largest Pacific watershed (~240,000 km^2), is a mountainous, mainly inland, nival basin (Figure 1). Streamflow over most of the FRB is dominated by snowmelt during the spring freshet: the main gaged outlet of the basin, at Hope, has never recorded an

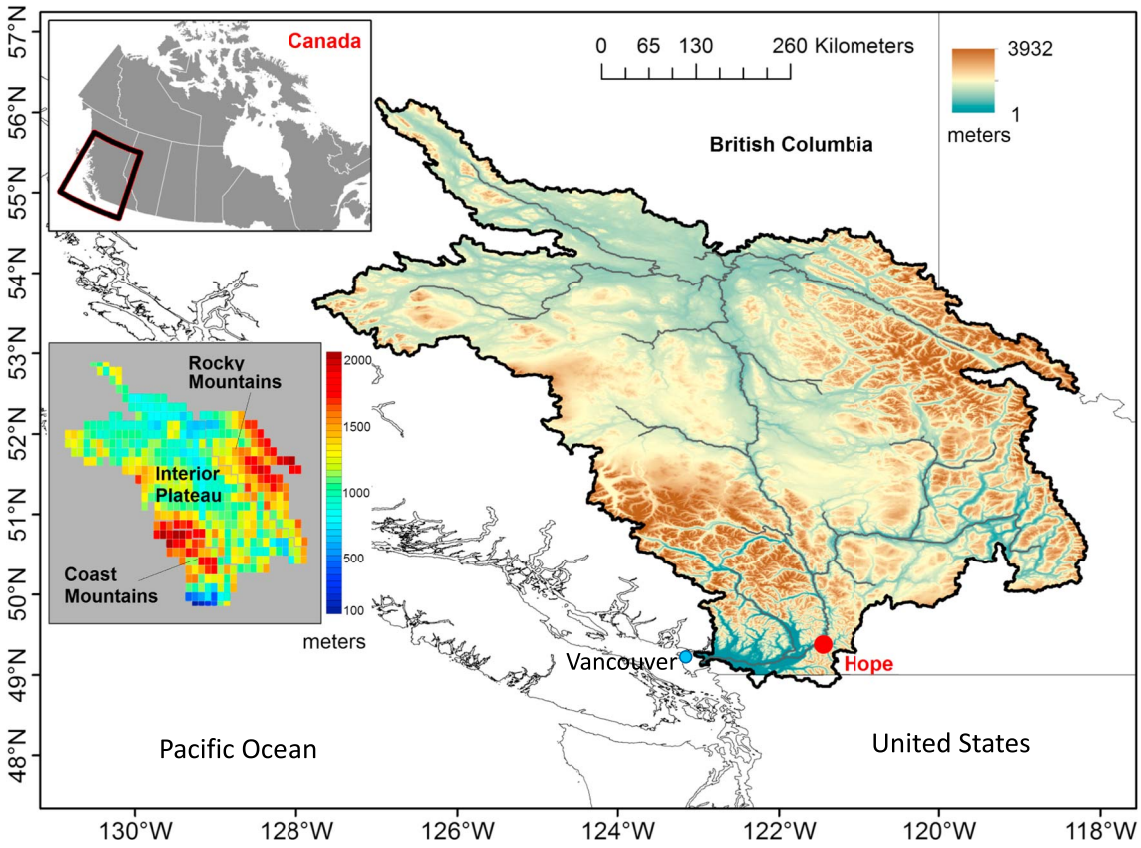

Figure 1. The Fraser River Basin. Elevation map showing location of the major basin gaging station at Hope. Upper inset: location of the Fraser River Basin within Canada. Lower inset: Variable Infiltration Capacity model grid, showing the horizontal resolution of 1/4° and geoclimatic regions.

annual peak daily flow (APF) outside of the April–July period (from 1912 to 2018). The western portion of the FRB is nevertheless affected by strong, seasonal incursions of moist air from the Pacific in fall and winter, often associated with cyclonic storms. These "atmospheric rivers" (ARs), large (>2000 km long by a few 100 km wide) plumes of lower tropospheric water vapor visible in satellite microwave images (Bao et al., 2006; Neiman et al., 2008), can make landfall anywhere along the West Coast of North America (American Meteorological Society, 2018). Ascending the Coast Mountains at the FRB's western boundary, this moist air condenses into orographic precipitation. ARs contribute disproportionately to cold season precipitation and streamflow: Dettinger et al. (2011) found that over the period 1951–2008, 15% (median; 22% maximum) of annual rainfall at stations in central and northern California originated from the most intense ARs, accounting for up to 32% (median; 55% maximum) of streamflow in the region. In the FRB, Spry et al. (2014), estimated that 11% of annual rainfall (two station mean; maximum 17%) and 16.5% of streamflow (one station mean; maximum 37%) were contributed by such storms during 1965–1985.

ARs have been diagnosed from vertically integrated water vapor (IWV) and/or horizontal water vapor transport (IVT) in observational reanalyses (Dettinger et al., 2011; Neiman et al., 2008; Payne & Magnusdottir, 2014) and models. Analyses of GCM simulations over western North America found statistically significant increases in future cold season (October–March) extreme IVT frequency, regardless of whether ARs are defined via exceedance of IWV/IVT thresholds (Dettinger, 2011; Gao et al., 2015; Payne & Magnusdottir, 2015; Warner et al., 2015), or characteristic spatial patterns (Radić et al., 2015). For instance, at a point just southwest of Vancouver Island, Warner et al. (2015) found a remarkable quadrupling in the exceedance frequency of the historical (1970–1999) 99th IVT percentile by 2070–2099, using a CMIP5 ensemble under Representative Concentration Pathway (RCP)8.5.

These studies and others (Hagos et al., 2016; Leung & Qian, 2009; Ralph et al., 2006) have associated ARs with heavy precipitation over western North America and also investigated their inland penetration

(Mahoney et al., 2018; Rutz et al., 2014), a relevant issue for the FRB. However, no work to date has investigated the indirect link, via precipitation and land hydrology, between future ARs and extreme streamflow, despite calls for a multimodel ensemble approach to do so (Salathé et al., 2014). Previous studies of projected FRB streamflow reported mixed results, with increased or decreased flows depending on the specific return period considered (Kerkhoven & Gan, 2011; Milly et al., 2002; Shrestha et al., 2017, 2012; Whitfield et al., 2002, 2003). By employing a 21-member CMIP5 ensemble to drive a process-based hydrologic model, we undertake a robust approach that directly addresses the implications of the changing frequency and intensity of ARs for extreme streamflow in the FRB and, by extension, other large nival basins.

2. Models and Methodology

2.1. GCM Ensemble and Hydrologic Model

Our modeling chain begins with daily maximum and minimum temperature and daily mean precipitation from 21 CMIP5 GCM simulations, driven by historical forcings up to 2005 and RCP8.5 from 2006 to 2100 (Figure S1 and Table S1 in the supporting information). These outputs were downscaled to high spatial resolution using a sophisticated statistical downscaling and bias correction method, which increases our confidence in derived future hydroclimatic changes (PCIC, 2016; Werner & Cannon, 2016; supporting information). The bias correction uses a daily gridded station data set for 1950–2010 produced by interpolating station data from Environment and Climate Change Canada observing sites onto a high-resolution grid using local elevation, longitude, and latitude as covariates (Hutchinson et al., 2009; supporting information).

These downscaled outputs, along with spatially interpolated daily 10-m wind speeds from the National Centers for Environmental Prediction/National Center for Atmospheric Research Reanalysis (Kalnay et al., 1996), were used to drive the VIC hydrological model (Liang et al., 1994) over the FRB from 1950 to 2099. Variable Infiltration Capacity (VIC) is applied at a horizontal resolution of 1/4° (~20–25 km, depending on latitude; Figure 1) and solves the one-dimensional water and energy balance equations within each grid cell at a daily time step (except for the snow submodel, which runs at hourly resolution). VIC uses varying topography and land cover, but land cover fractions are unchanged throughout the simulations. Surface runoff and subsurface flow are generated at each grid cell and directed into a surface routing network (Lohmann et al., 1996, 1998); simulated streamflow is subsequently extracted at the grid cell representing Hope. VIC was calibrated and validated using daily streamflow measurements at several locations, as described by Islam et al. (2017). VIC-simulated annual extreme streamflow was evaluated by comparing the results of a simulation driven by gridded observational data spanning 1956–2006 to discharge measurements at Hope (Water Survey of Canada, 2016). Quantile plots (Figure S2) reveal that the VIC-simulated APF and annual peak flow date (APD) are indistinguishable from observations at the 5% significance level. The creation of a large ensemble of VIC simulations driven by different downscaled GCMs allows assessment of the magnitude of forced changes compared with model uncertainty.

2.2. Analysis of Extreme Values and Exceedance Probability

Streamflow at Hope was analyzed in decadal blocks from 1960–1969 to 2090–2099, omitting the first decade of VIC model spin-up. APF and APD were extracted for each year and model run of the ensemble, resulting in 210 values for each decade. Under the assumptions a that each decadal set is roughly stationary (confirmed a posteriori) and that APFs from different driving models share roughly the same distribution (Conover, 1999; supporting information section S3), we fit a generalized extreme value (GEV) distribution to the APFs

$$\begin{aligned} G(z) &= \exp\left\{-\left[1+\xi\left(\frac{z-\mu}{\sigma}\right)\right]^{-\frac{1}{\xi}}\right\}, \qquad \xi \neq 0 \\ &= \exp\left\{-\exp\left[-\left(\frac{z-\mu}{\sigma}\right)\right]\right\}, \qquad \xi = 0, \end{aligned} \tag{1}$$

where z is the APF and (μ, σ, ξ) are the location, scale, and shape parameters, respectively, of the GEV distribution (Coles, 2001). These parameters were estimated by the method of L-moments (Hosking, 1990),

using the extRemes package in the R programming environment (Gilleland & Katz, 2016; R Core Team, 2018). From the fitted distribution, return levels z_p and periods $1/p$ are calculated by inverting equation (1)

$$\begin{aligned} z_p &= \mu - \frac{\sigma}{\xi}\left[1-\{-\log(1-p)\}^{-\xi}\right], \quad \xi \neq 0, \\ &= \mu - \sigma \log\{-\log(1-p)\}, \quad \xi = 0, \end{aligned} \tag{2}$$

where $G(z_p) = 1 - p$. The function $z_p(1/p)$, also known as a flood frequency curve, has the interpretation that an APF of magnitude z_p is exceeded on average once every $1/p$ years.

We also calculate the conditional exceedance probability for pairs of variables. For two daily variables $x(t)$ and $y(t)$, we evaluate (1) the probability that x exceeds a specified value X on days t^* when y exceeds some threshold y^*, that is, $P((x > X)|y > y^*)$ and (2) the probability that $x > X$ on all other days. These were estimated as follows:

$$P\left((x>X)|y>y^*\right) = 1 - F\left[x\left(t^*\right)\right] \quad \text{and} \quad P\left((x>X)|y\leq y^*\right) = 1 - F\left[x\left(t\neq t^*\right)\right], \tag{3}$$

respectively, where F is the empirical cumulative distribution function computed from the appropriate subset of x.

2.3. AR Definition

There are varying definitions of ARs in the literature. Given the dual drivers of AR behavior (IWV and wind), a definition comprising the exceedance of a high percentile threshold of IVT is increasingly used, with thresholds ranging from the 85th percentile of IVT (Gao et al., 2015; Lavers et al., 2012; Payne & Magnusdottir, 2015) to the 99th percentile (Warner et al., 2015). We computed IVT within the lower troposphere from the daily CMIP5 model output as

$$\text{IVT}\ \left(\text{kg m}^{-1}\text{s}^{-1}\right) = \frac{1}{g}\int_{\text{surface}}^{500\ \text{hPa}} \overline{q}\overline{v}\,dp \tag{4}$$

at each GCM grid cell, where $g = 9.81$ m/s^2, $\overline{q}$ (kg/kg) is the specific humidity, $\overline{v}$ (m/s) is the wind speed (means over a specified GCM vertical layer), and we omit levels above 500 hPa, whose contributions are negligible (Gao et al., 2015). At the surface, pressure p_s, q_s, and v_s are additional spatiotemporal variables. We use the 95th percentile of IVT, IVT95, over the historical period 1980–2009 to identify AR events for the reasons discussed in section 4.2.

3. Results of the CMIP5-VIC Simulations

3.1. Streamflow Extremes From Present to Future

While the vast majority of APFs occur during the freshet season (1 April to 31 July) in the model-simulated historical period (1980–2009, hereafter 1990s), a small fraction (17 out of 630 or 2.7%) occurs at other times; these are termed nonfreshet peak flows or NPFs (Figure 2a). NPFs occur in 10 models, with discharge magnitudes ranging from 5,000 to 10,000 m^3/s (mean $\pm$ 1σ = 8,536 $\pm$ 1,976 m^3/s). Further analysis reveals that the NPFs are generated by substantial rainfall episodes occurring within their host GCMs, in years when the snowmelt-generated flow is unusually low compared with other models (and compared to observations). While the magnitude and spatial pattern of temperature and precipitation entering VIC are constrained via the downscaling method (supporting information), snow accumulation and melt are generated within VIC. Hence, biases in simulated snowmelt runoff can occur.

Substantial changes in APF timing and magnitude are seen by the late 21st century (Figure 2b). Chief among these are the following: (1) Many more NPFs occur in future, with a total of 167 (27% of APFs) over all simulations during 2070–2099. APFs occur throughout the year, except July–August. (2) A small number of NPFs exceed 15,200 m^3/s, the largest recorded daily discharge at Fraser-Hope (1948, more than three standard deviations higher than the mean simulated 1980–2009 APF). NPFs occur across all CMIP5 driving models by the 2080s (Figure S3). There is some suggestion that the CMIP5 GCMs generating the largest number of NPFs in the 2080s are affected by large errors in atmospheric feedbacks governing the El Niño–Southern Oscillation (4 out of 5—and 7 of 10—GCMs generating the largest number of NPFs in future have high "feedback score" errors, according to Bellenger et al. (2014)).

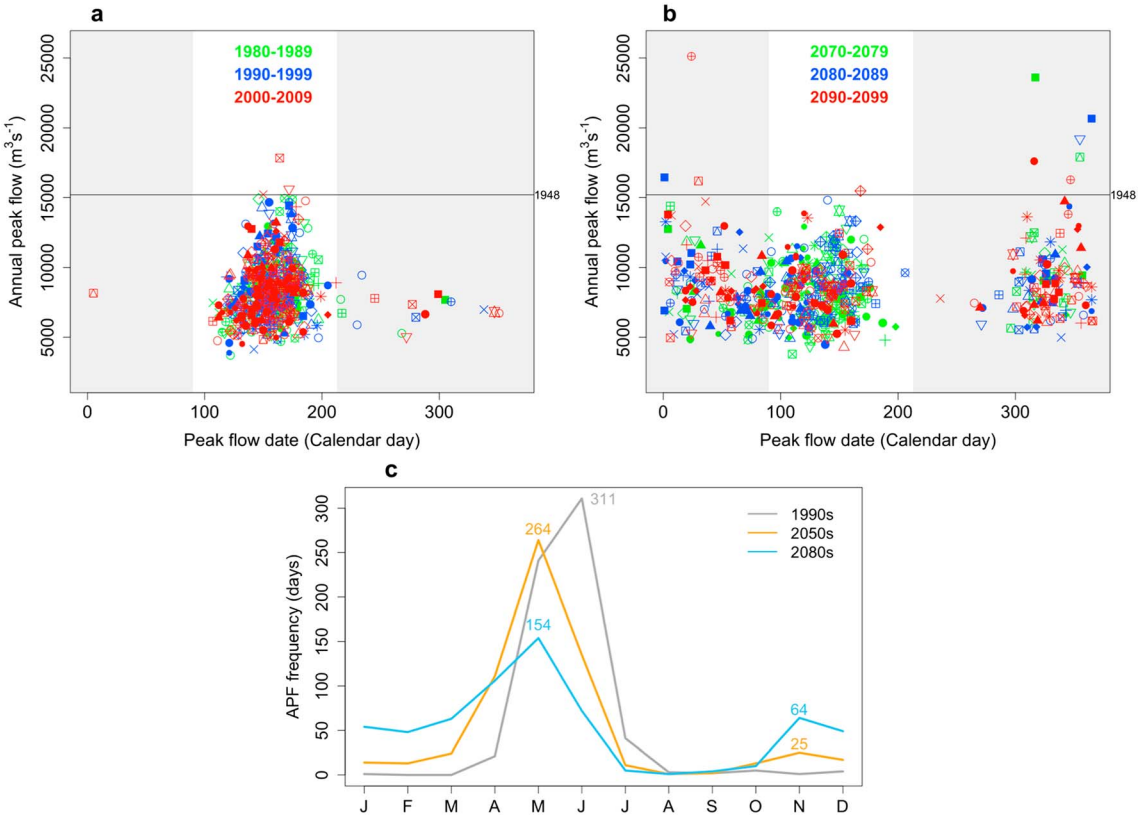

Figure 2. Scatter plots of APF versus annual peak flow date at Hope for the Coupled Model Intercomparison Project Phase 5-Variable Infiltration Capacity model-simulated (a) historical (1980–2009) and (b) future (2070–2099) periods, with distinct colors for each decade and symbols for each simulation. Gray shading indicates the non-freshet season, that is, 1 August to 31 March. The highest recorded flow level (1948) is shown by a horizontal line. (c) "Frequency hydrograph", i.e., sum of the monthly occurrence of APFs across all years and simulations, for the three 30-year periods: 1980–2009, 2040–2069 and 2070–2099. APF = annual peak daily flow.

3.2. Flood Frequency Analysis

The presence of several NPFs exceeding the historical maximum in Figure 2b suggests using flood frequency analysis to estimate the likelihood of comparable future events using the CMIP5-VIC ensemble. We performed GEV fits on both annual (Figures 3a and 3b) and cold season (Figures 3c and 3d) streamflow maxima (section 2.2). Aside from a slight underestimate of return levels for the most frequent events, most return periods z_p estimated for 1980–1989 are in good agreement with the flood frequency curve constructed from gauge observations (1955–2014) centered on the same decade (Figure 3a). No significant change in return values is projected for 2050–2059, although interdecadal variability in z_p is large at the longest return periods (e.g., Q100 in Figure 3b). By contrast, a notable increase occurs in z_p by the late 21st century (2090–2099), so that a Q100 event in 1980–1989 becomes roughly a Q20 event in 2090–2099. The same results imply that the magnitude of a 100-year flood increases by 27% by the end of the 21st century relative to 1980–1989, albeit with a large uncertainty (12–46%; Figure 3a). By the 2070s, the 100-year return level exceeds the largest recorded APF at Hope in 1948 (Figure 3b).

Historically, cold season flows at Fraser-Hope are limited by freezing temperatures upstream over much of October–March. The estimated Q100 return value is less than 5,000 m^3/s (Figure 3c; results from 1955 to 2014 are shown in the figure; use of the longer record from 1912 gives a similar result). VIC overestimates z_p over the cold season, with the discrepancy widening at the longest periods (dots versus curves in Figure 3d). Since VIC does not exhibit this bias when driven by observations (Curry & Zwiers, 2018), it is likely caused by the anomalous NPFs generated by a handful of CMIP5-VIC simulations in the historical period (Figure 2a). In contrast to the annual case, z_p at all return periods is substantially larger than historical values by the mid-21st century (Figure 3c). However, the 100-year cold season z_p again approaches the

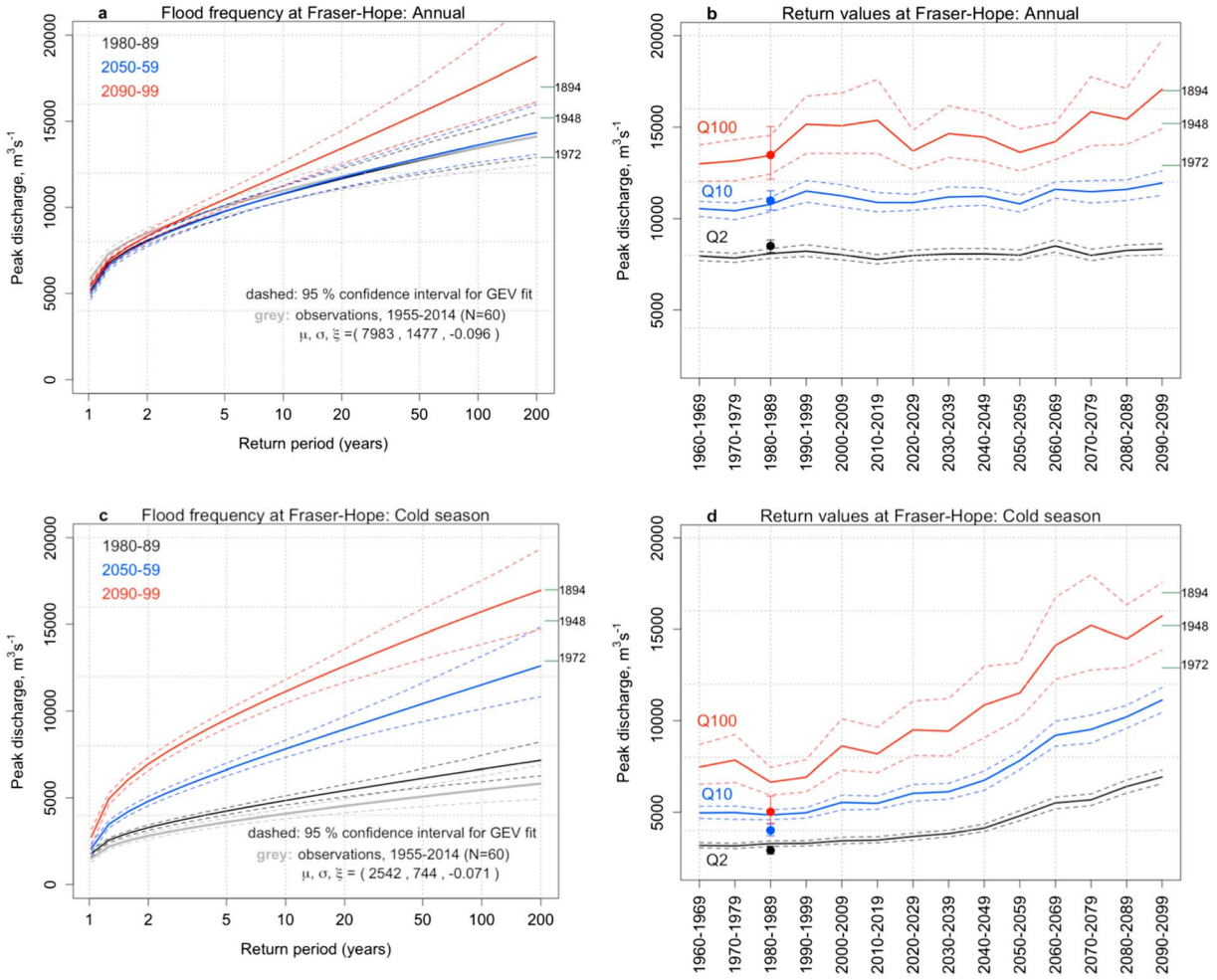

Figure 3. (a) Flood frequency plot of results from GEV fitting of annual peak daily flow for three decades. The (b) 2-year (Q2), 10-year (Q10), and 100-year (Q100) return period peak flow projections. Dashed lines show 2.5% and 97.5% confidence intervals. Large dots indicate the Q2, Q10, and Q100 values derived from observations over the period 1955–2014 (plotted at the central decade of the 1980s), with error bars showing the same confidence intervals. (c, d) Same as in (a, b) but for October to March. In each panel, the two highest recorded flow levels (1948, 1972) are shown on the right-hand axis, along with the estimated (pregage) flow from 1894 (Curry & Zwiers, 2018). GEV = generalized extreme value.

record annual 1948 level at Hope by the 2070s. Compared to 1980–2009, the Q2, Q10, and Q100 cold season return levels are each projected to approximately double by 2070–2099. These large increases exemplify the future nival to nival/pluvial transformation in the FRB. While large precipitation events occur throughout the simulations, in the historical period they result predominantly in snowfall and thus storage until the freshet. In future, an increasing fraction of precipitation falls as rain and enters the river network essentially instantaneously as runoff, fundamentally changing the seasonal pattern of streamflow.

4. Causes of the Hydrologic Regime Shift

4.1. Projected Changes in Precipitation, Extreme Rainfall, and Streamflow

The most important large-scale climatic drivers in the CMIP5 simulations over the FRB are (1) cold season (October–March) warming of ~4–5 °C, which reduces the snow-to-rain ratio below unity as the 0 °C threshold is exceeded (Figure S5) and (2) cold season precipitation increases of ~10–20% (both results for 2070–2099 versus 1980–2009, obtained from 39 CMIP5-RCP 8.5 runs; KNMI Climate Explorer, 2018). The CMIP5-VIC simulations display decreasing snowfall and increasing rainfall throughout the 21st century, especially in autumn (Figure S5; Islam et al., 2019). The largest rainfall increases are seen in October through January, with peak increases of 62 mm (110%) in November and 44 mm (137%) in December from the 1990s

to the 2080s (median model results; Figure S6a). Significant changes in extreme rainfall also occur. Taking the 99th percentile of daily rainfall in the 1980–2009 period (R99) as a measure of such an extreme, we computed its exceedance frequency, *N*(R99x), across the ensemble. By the 2080s, all months except August showed an increase in *N*(R99x), with November having the largest increase of 1.7 additional R99x days in the future (multimodel mean; Figure S6b). Cold season *N*(R99x) is projected to nearly quadruple from the 1990s to the 2080s. Furthermore, multiday R99x events (defined as instances of consecutive R99x days) increase in absolute and relative frequency. A 3-day event that occurred less than once a year in the 1990s occurs with a frequency of 3.1 year^{-1} in the 2050s and 5.3 year^{-1} in the 2080s, while a handful of unprecedented 5- and 6-day R99x events occur by the 2050s.

Reduced spring freshet flows are a robust feature of transient hydroclimate model projections conducted in a host of nival basins including the FRB (Morrison et al., 2002; Shrestha et al., 2012), yet the emergence of NPFs is not typically predicted. Their emergence in this study is linked to more frequent heavy rainfall episodes in the cold season, which are best captured at the daily timescale. To see this, we first compared the time series of R99x for each period to that of APD from the simulated streamflow time series at Hope, to identify occurrences of R99x falling within a 10-day period prior to each year's APD. This lag allows for the fact that R99x describes basin-averaged rainfall and also that the transport time from the headwaters of the FRB to Hope is up to a week (Carver et al., 2009). We then stratified the results by freshet and nonfreshet flow seasons.

The fraction of R99x-related NPFs increases from 3% in the 1990s, to 24% (2050s) and, remarkably, to 67% (2080s; Table S2). Freshet peak flows are also associated with heavy rainfall events, with the joint occurrence ranging from 21% to 26%, but do not exhibit a clear trend over time. Overall, R99x-APF associations more than triple by the 2080s.

We also examined the probability of cold season discharge conditional on the occurrence of a R99x event, *P*(*Q*|R99x) (equation (3)). Using a subset of nine CMIP5 driving models examined further in section 4.2 (Table S1) and allowing for a lag of up to 5 days in the streamflow response, we found (Figure S7) that (i) discharge is significantly larger in 2070–2099 than in 1980–2009, irrespective of rainfall magnitude, (ii) discharge on R99x days is larger than on nonextreme rainfall days, and (iii) future discharge on R99x days is substantially larger than on historical R99x days. These characteristics hold across the model subset.

4.2. Link to ARs

Given projected increases in the frequency of extreme IVT events in the CMIP5 models and the strong historical association of ARs with heavy precipitation on the BC coast (section 1), we now investigate possible links between AR frequency, rainfall, and NPFs in the CMIP5-VIC simulations. We selected a subset of nine GCMs from our CMIP5-VIC ensemble (Table S1) and computed daily IVT from the model output according to equation (4). Four of these GCMs were assessed as "high-performing" models with respect to their reproduction of IVT, its components, and AR frequency compared to reanalysis by Payne and Magnusdottir (2015; who identified seven such GCMs). Their identification of a similar number of poorly performing models guided our decision to limit consideration to nine GCMs while still allowing assessment of intermodel variability. Following previous authors, we computed IVT at a small number of ocean grid points southwest of the FRB, and also at Hope, to represent ARs before and after landfall. Using 10 CMIP5 GCMs (three in common with our subset), Warner et al. (2015) and Warner and Mass (2017) demonstrated that composites of IVT99x (i.e., IVT > IVT99) events at specific grid points along a coastal transect in the historical period were invariably part of more extended AR-like structures trailing thousands of kilometers southwest into the Pacific. Payne and Magnusdottir (2014), who tracked the centroids of AR plumes defined using IVT85 and IVT95 percentile thresholds backward in time using satellite data, found similar results. Hence, we analyze the IVT interpolated to the location of Hope (49.39°N, 121.44°W), using the IVT95x definition of an AR. At this location, IVT95x ranges from 209 to 377 kg m^{-1} s^{-1}, depending on the model, with all but one model exceeding the fixed IVT threshold of 250 kg m^{-1} s^{-1} adopted by Dettinger (2011) and Rutz et al. (2014) for an AR.

An examination of *P*(*R*|IVT95x) across the subset of nine CMIP5 driving models shows that daily rainfall is generally larger in future, irrespective of IVT magnitude (a lag of 0–3 days was used; Figure S8). However, rainfall on IVT95x days is usually larger than on nonextreme IVT days (eight of nine models in 1980–2009 and six of nine models in 2070–2099), while rainfall on IVT95x days in the future is substantially larger than on IVT95x days in the past (seven of nine models). IVT95x days in the historical period account for 17–46%

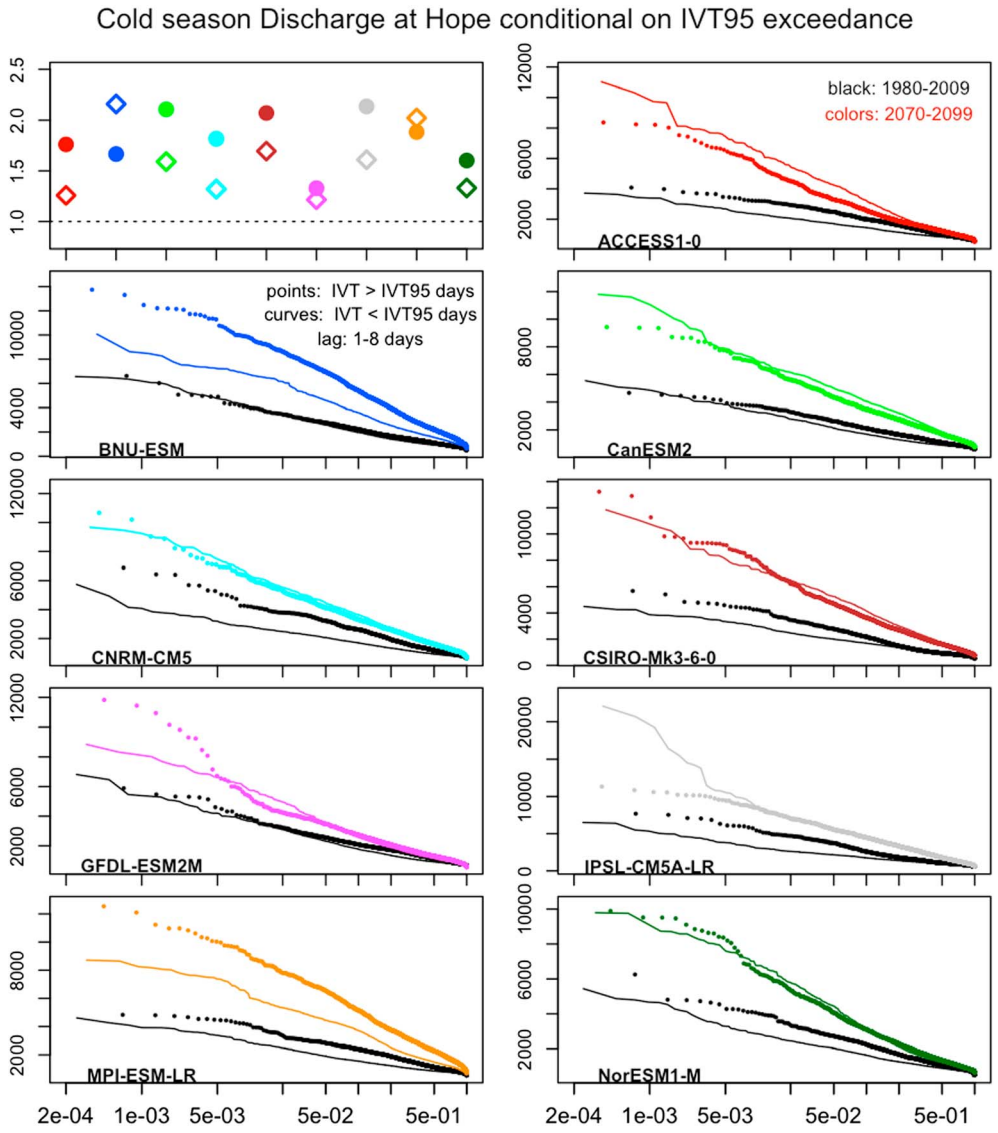

Figure 4. Conditional exceedance probability (*x* axis) for Variable Infiltration Capacity model-simulated, cold season daily discharge (*y* axis, $m^3\ s^{-1}$) across a subset of Coupled Model Intercomparison Project Phase 5 driving models. Points are for a period of 1–8 days after an IVT95x occurrence (with IVT95 calculated over 1980–2009); curves are for all other days. Black curves and points are for 1980–2009, colors for 2070–2099. Upper left panel: Ratio of future-to-historical average discharge on IVT95x days (open diamonds) and on non-IVT95x days (filled circles).

(nine model mean: 31%) of total cold season rainfall, increasing to 27–60% (mean: 38%) in the 2080s, suggesting a firm connection between the increased future occurrence of AR days and corresponding increases in daily rainfall.

Next we examined the exceedance probability of discharge conditional on the occurrence of IVT95x, that is, *P*(*Q*|IVT95x), applying a lag of 1–8 days for the rainfall-streamflow response to IVT95x (results are insensitive to the choice of slightly different intervals). Figure 4 demonstrates that (i) discharge is notably larger in 2070–2099 (colored curves) than in 1980–2009 (black curves), irrespective of IVT (upper left panel), (ii) discharge on IVT95x days in the future is substantially larger than in the past, and (iii) discharge on IVT95x days (points) is usually larger than on nonextreme IVT days (curves). While there are exceptions (e.g., future discharge on IVT95x days is lower than on normal IVT days in ACCESS1-0, CanESM2, IPSL-CM5-LR, and at low *Q* in a few models), these characteristics hold for a majority of the models examined, particularly at high *Q*. The mean *Q* on non-IVT95x days increases more than on IVT95x days in future (Figure 4, upper left),

implying that despite increased rainfall from ARs, the state of the snowpack is likely still important for moderating streamflow. Additional tests were applied to check the sensitivity of our results to the IVT calculation method (supporting information section S4). In summary, these results strongly suggest that the increased frequency of future cold season streamflow extremes is due to the projected increase in landfalling ARs along the BC coast.

5. Discussion and Conclusions

Despite clear relationships between IVT95x and rainfall on the one hand (section 4.2) and R99x and streamflow on the other (section 4.1), $P(Q|\text{IVT95x})$ exhibits considerable variability over the multimodel ensemble. The frequency of heavy precipitation varies among GCMs, while its effect on runoff depends on the spatial distribution of antecedent snowpack, soil moisture, topography, baseflow, and the routing network in the hydrologic model. Further investigation of the partitioning of surface water between the atmosphere, snowpack, and soil within the hydrologic model during AR events would help clarify the relationship of extreme IVT to streamflow.

One possible concern with our modeling framework is that VIC was calibrated using present-day, snowmelt-dominated conditions in the FRB but subsequently used to assess the consequences of a regime shift in precipitation phase. However, VIC has been applied to pluvial and mixed nival-pluvial basins (Das et al., 2011; Tohver et al., 2014) and calibrated using a range of wet, dry, and average years (Schnorbus et al., 2014). Perhaps more importantly, errors in the simulation of precipitation within the CMIP5 GCMs (even after bias adjustment), such as those leading to NPFs in the historical period (section 3.1), still limit our confidence in hydroclimatic projections.

Our conclusion that more frequent AR-driven precipitation events in future prompt much larger cold season flows may warrant a reconsideration of flood plans in the FRB and similarly exposed basins. While regional emergency-preparedness plans often focus on historic "floods of record," it may be more germane to consider a scenario wherein a sequence of AR-driven storms impacts the region in succession, as considered by Dettinger et al. (2012). Combined with small-scale, hydraulic modeling, this approach could lead to valuable design guidelines for a variety of watercourses and control structures in vulnerable catchments.

Acknowledgments
We acknowledge the World Climate Research Programme's Working Group on Coupled Modeling, which is responsible for CMIP5, and thank the climate modeling groups for producing and making available their GCM output. For CMIP, the U.S. Department of Energy's Program for Climate Model Diagnosis and Intercomparison provides coordinating support and led development of software infrastructure in partnership with the Global Organization for Earth System Science Portals. The CMIP5 model output data are available via https://cmip.llnl.gov/cmip5/data_portal.html. A portion of the CMIP5 output was obtained from the Center for Environmental Data Analysis at Natural Environment Research Council's Data Repository for Atmospheric Science and Earth Observation (UK), which is available at http://data.ceda.ac.uk/badc/cmip5/. We thank Stephen Sobie for clarification of the BCCAQ2 method, Michael Warner for sharing unpublished results from his work, Yaheng Tan and Christian Seiler for sharing CMIP5 output from the Earth System Grid Federation, and Markus Schnorbus for reviewing the draft manuscript. The constructive comments of two reviewers led to an improved presentation of the results. Charles Curry and Siraj Ul Islam were supported by the NSERC-funded Canadian Sea Ice and Snow Evolution (CanSISE) Network.

References

American Meteorological Society (2018). "Atmospheric river". Glossary of meteorology. Retrieved from http://glossary.ametsoc.org/wiki/Atmospheric_river

Bao, J. W., Michelson, S. A., Neiman, P. J., Ralph, F. M., & Wilczak, J. M. (2006). Interpretation of enhanced integrated water vapor bands associated with extratropical cyclones: Their formation and connection to tropical moisture. *Monthly Weather Review*, *134*(4), 1063–1080. https://doi.org/10.1175/MWR3123.1

Bellenger, H., Guilyardi, É., Leloup, J., Lengaigne, M., & Vialard, J. (2014). ENSO representation in climate models: From CMIP3 to CMIP5. *Climate Dynamics*, *42*(7-8), 1999–2018. https://doi.org/10.1007/s00382-013-1783-z

Carver, M., Weiler, M., Scheffler, C., & Rosin, K. (2009). Development and application of a peak-flow hazard model for the Fraser basin (British Columbia). MPBI Project #7.29, Natural Resources Canada, Canadian Forest Service. Retrieved from http://www.cfs.nrcan.gc.ca/pubwarehouse/pdfs/31187.pdf

Coles, S. (2001). *An introduction to statistical modeling of extreme values* (p. 208). London: Springer. https://doi.org/10.1007/978-1-4471-3675-0

Collins, M., & Knutti, R. (2013). Chapter 12: Long-term climate change: Projections, commitments and irreversibility–final draft, underlying scientific–technical assessment. In T. F. Stocker, et al. (Eds.), *Working group 1 contribution to the IPCC fifth assessment report: Climate change 2013: The physical science basis* (pp. 1029–1136). Cambridge: Cambridge University Press.

Conover, W. J. (1999). *Practical nonparametric statistics* (3rd ed.). New York: Wiley.

Curry, C. L., & Zwiers, F. W. (2018). Examining controls on peak annual streamflow and floods in the Fraser River Basin of British Columbia. *Hydrology and Earth System Sciences*, *22*(4), 2285–2309. https://doi.org/10.5194/hess-22-2285-2018

Das, T., Dettinger, M. D., Cayan, D. R., & Hidalgo, H. G. (2011). Potential increase in floods in California's Sierra Nevada under future climate projections. *Climatic Change*, *109*(S1), 71–94. https://doi.org/10.1007/s10584-011-0298-z

Dettinger, M. D. (2011). Climate change, atmospheric rivers, and floods in California—A multimodel analysis of storm frequency and magnitude changes. *Journal of the American Water Resources Association (JAWRA)*, *47*(3), 514–523. https://doi.org/10.1111/j.1752-1688.2011.00546.x

Dettinger, M. D., Ralph, F. M., Das, T., Neiman, P. J., & Cayan, D. (2011). Atmospheric rivers, floods, and the water resources of California. *Water*, *3*(2), 445–478. https://doi.org/10.3390/w3020445

Dettinger, M. D., Ralph, F. M., Hughes, M., Das, T., Neiman, P., Cox, D., et al. (2012). Design and quantification of an extreme winter storm scenario for emergency preparedness and planning exercises in California. *Natural Hazards*, *60*(3), 1085–1111. https://doi.org/10.1007/s11069-011-9894-5

Gao, Y., Lu, J., Leung, L. R., Yang, Q., Hagos, S., & Qian, Y. (2015). Dynamical and thermodynamical modulations on future changes of landfalling atmospheric rivers over western North America. *Geophysical Research Letters*, *42*, 7179–7186. https://doi.org/10.1002/2015GL065435

Gilleland, E., & Katz, R. W. (2016). extRemes 2.0: An extreme value analysis package in R. *Journal of Statistical Software*, *72*(8), 1–39.
Hagos, S. M., Leung, L. R., Yoon, J. H., Lu, J., & Gao, Y. (2016). A projection of changes in landfalling atmospheric river frequency and extreme precipitation over western North America from the large ensemble CESM simulations. *Geophysical Research Letters*, *43*, 1357–1363. https://doi.org/10.1002/2015GL067392
Hanzer, F., Förster, K., Nemec, J., & Strasser, U. (2018). Projected cryospheric and hydrological impacts of 21st century climate change in the Ötztal Alps (Austria) simulated using a physically based approach. *Hydrology and Earth System Sciences*, *22*(2), 1593–1614. https://doi.org/10.5194/hess-22-1593-2018
Hosking, J. R. M. (1990). L-Moments: Analysis and estimation of distributions using linear combinations of order statistics. *Journal of the Royal Statistical Society, Series B*, *52*, 105–124.
Hutchinson, M. F., McKenney, D. W., Lawrence, K., Pedlar, J. H., Hopkinson, R. F., Milewska, E., & Papadopol, P. (2009). Development and testing of Canada-wide interpolated spatial models of daily minimum–maximum temperature and precipitation for 1961–2003. *Journal of Applied Meteorology and Climatology*, *48*(4), 725–741. https://doi.org/10.1175/2008JAMC1979.1
Islam, S. U., Déry, S. J., & Werner, A. T. (2017). Future climate change impacts on snow and water resources of the Fraser River Basin, British Columbia. *Journal of Hydrometeorology*, *18*(2), 473–496. https://doi.org/10.1175/JHM-D-16-0012.1
Islam, S. U., Curry, C. L., Déry, S. J., & Zwiers, F. W. (2019). Quantifying projected changes in runoff variability and flow regimes of the Fraser River Basin, British Columbia. *Hydrology and Earth System Sciences*, *23*, 1–18. https://doi.org/10.5194/hess-23-1-2019
Kalnay, E., Kanamitsu, M., Kistler, R., Collins, W., Deaven, D., Gandin, L., et al. (1996). The NCEP/NCAR 40-year reanalysis project. *Bulletin of the American Meteorological Society*, *77*(3), 437–471. https://doi.org/10.1175/1520-0477(1996)077<0437:TNYRP>2.0.CO;2
Kerkhoven, E., & Gan, T. Y. (2011). Differences and sensitivities in potential hydrologic impact of climate change to regional-scale Athabasca and Fraser River basins of the leeward and windward sides of the Canadian Rocky Mountains respectively. *Climatic Change*, *106*(4), 583–607. https://doi.org/10.1007/s10584-010-9958-7
KNMI Climate Explorer (2018). Retrieved from https://climexp.knmi.nl/plot_atlas_form.py
Krasting, J. P., Broccoli, A. J., Dixon, K. W., & Lanzante, J. R. (2013). Future changes in Northern Hemisphere snowfall. *Journal of Climate*, *26*(20), 7813–7828. https://doi.org/10.1175/JCLI-D-12-00832.1
Kundzewicz, Z. W., Mata, L. J., Arnell, N. W., Döll, P., Kabat, P., Jiménez, B., et al. (2007). Freshwater resources and their management. In M. L. Parry, O. F. Canziani, J. P. Palutikof, P. J. van der Linden, & C. E. Hanson (Eds.), *Climate change 2007: Impacts, adaptation and vulnerability. Contribution of working group II to the fourth assessment report of the intergovernmental panel on climate change* (pp. 173–210). Cambridge: Cambridge University Press.
Lavers, D. A., Villarini, G., Allan, R. P., Wood, E. F., & Wade, A. J. (2012). The detection of atmospheric rivers in atmospheric reanalyses and their links to British winter floods and the large-scale climatic circulation. *Journal of Geophysical Research*, *117*, D20106. https://doi.org/10.1029/2012JD018027
Leung, L. R., & Qian, Y. (2009). Atmospheric rivers induced heavy precipitation and flooding in the western US simulated by the WRF regional climate model. *Geophysical Research Letters*, *36*, L03820. https://doi.org/10.1029/2008GL036445
Liang, X., Lettenmaier, D. P., Wood, E. F., & Burges, S. J. (1994). A simple hydrologically based model of land surface water and energy fluxes for general circulation models. *Journal of Geophysical Research*, *99*(D7), 14,415–14,428. https://doi.org/10.1029/94JD00483
Lohmann, D., Nolte-Holube, R., & Raschke, E. (1996). A large-scale horizontal routing model to be coupled to land surface parametrization schemes. *Tellus A*, *48*(5), 708–721. https://doi.org/10.3402/tellusa.v48i5.12200
Lohmann, D., Raschke, E., Nijssen, B., & Lettenmaier, D. P. (1998). Regional scale hydrology: I. Formulation of the VIC-2L model coupled to a routing model. *Hydrological Sciences Journal*, *43*(1), 131–141. https://doi.org/10.1080/02626669809492107
Mahoney, K., Swales, D., Mueller, M., Alexander, M., Hughes, M., & Malloy, K. (2018). An examination of an inland-penetrating atmospheric river flood event under potential future thermodynamic conditions. *Journal of Climate*, *31*(16), 6281–6297. https://doi.org/10.1175/JCLI-D-18-0118.1
Milly, P. C. D., Wetherald, R. T., Dunne, K. A., & Delworth, T. L. (2002). Increasing risk of great floods in a changing climate. *Nature*, *415*(6871), 514–517. https://doi.org/10.1038/415514a
Morrison, J., Quick, M. C., & Foreman, M. G. (2002). Climate change in the Fraser River watershed: Flow and temperature projections. *Journal of Hydrology*, *263*(1-4), 230–244. https://doi.org/10.1016/S0022-1694(02)00065-3
Neiman, P. J., Ralph, F. M., Wick, G. A., Lundquist, J. D., & Dettinger, M. D. (2008). Meteorological characteristics and overland precipitation impacts of atmospheric rivers affecting the West Coast of North America based on eight years of SSM/I satellite observations. *Journal of Hydrometeorology*, *9*(1), 22–47. https://doi.org/10.1175/2007JHM855.1
Payne, A. E., & Magnusdottir, G. (2014). Dynamics of landfalling atmospheric rivers over the North Pacific in 30 years of MERRA reanalysis. *Journal of Climate*, *27*(18), 7133–7150. https://doi.org/10.1175/JCLI-D-14-00034.1
Payne, A. E., & Magnusdottir, G. (2015). An evaluation of atmospheric rivers over the North Pacific in CMIP5 and their response to warming under RCP 8.5. *Journal of Geophysical Research: Atmospheres*, *120*, 11,173–11,190. https://doi.org/10.1002/2015JD023586
PCIC (2016). ClimDown package, Pacific Climate Impacts Consortium. Retrieved from https://www.pacificclimate.org/resources/software-library, http://cran.r-project.org/web/packages/ClimDown/
Pierce, D. W., & Cayan, D. R. (2013). The uneven response of different snow measures to human-induced climate warming. *Journal of Climate*, *26*(12), 4148–4167. https://doi.org/10.1175/JCLI-D-12-00534.1
R Core Team (2018). R: A language and environment for statistical computing. R Foundation for Statistical Computing, Vienna, Austria. Retrieved from https://www.R-project.org/
Radić, V., Cannon, A. J., Menounos, B., & Gi, N. (2015). Future changes in autumn atmospheric river events in British Columbia, Canada, as projected by CMIP5 global climate models. *Journal of Geophysical Research: Atmospheres*, *120*, 9279–9302. https://doi.org/10.1002/2015JD023279
Ralph, F. M., Neiman, P. J., Wick, G., Gutman, S., Dettinger, M., Cayan, D., & White, A. B. (2006). Flooding on California's Russian River—Role of atmospheric rivers. *Geophysical Research Letters*, *33*, L13801. https://doi.org/10.1029/2006GL026689
Roderick, M. L., Sun, F., Lim, W. H., & Farquhar, G. D. (2014). A general framework for understanding the response of the water cycle to global warming over land and ocean. *Hydrology and Earth System Sciences*, *18*(5), 1575–1589. https://doi.org/10.5194/hess-18-1575-2014
Rutz, J. J., Steenburgh, W. J., & Ralph, F. M. (2014). Climatological characteristics of atmospheric rivers and their inland penetration over the western United States. *Monthly Weather Review*, *142*(2), 905–921. https://doi.org/10.1175/MWR-D-13-00168.1
Salathé, E. P. Jr., Hamlet, A. F., Mass, C. F., Lee, S. Y., Stumbaugh, M., & Steed, R. (2014). Estimates of twenty-first-century flood risk in the Pacific Northwest based on regional climate model simulations. *Journal of Hydrometeorology*, *15*(5), 1881–1899. https://doi.org/10.1175/JHM-D-13-0137.1

Schnorbus, M., Werner, A., & Bennett, K. (2014). Impacts of climate change in three hydrologic regimes in British Columbia, Canada. *Hydrological Processes*, *28*(3), 1170–1189. https://doi.org/10.1002/hyp.9661

Shrestha, R. R., Cannon, A. J., Schnorbus, M. A., & Zwiers, F. W. (2017). Projecting future nonstationary extreme streamflow for the Fraser River, Canada. *Climatic Change*, *145*(3–4), 289–303. https://doi.org/10.1007/s10584-017-2098-6

Shrestha, R. R., Schnorbus, M. A., Werner, A. T., & Berland, A. J. (2012). Modelling spatial and temporal variability of hydrologic impacts of climate change in the Fraser River basin, British Columbia, Canada. *Hydrological Processes*, *26*(12), 1840–1860. https://doi.org/10.1002/hyp.9283

Spry, C. M., Kohfeld, K. E., Allen, D. M., Dunkley, D., & Lertzman, K. (2014). Characterizing pineapple express storms in the lower mainland of British Columbia, Canada. *Canadian Water Resources Journal*, *39*(3), 302–323. https://doi.org/10.1080/07011784.2014.942574

Taylor, K. E., Stouffer, R. J., & Meehl, G. A. (2012). An overview of CMIP5 and the experimental design. *Bulletin of the American Meteorological Society*, *93*(4), 485–498. https://doi.org/10.1175/BAMS-D-11-00094.1

Tohver, I. M., Hamlet, A. F., & Lee, S.-Y. (2014). Impacts of 21st-century climate change on hydrologic extremes in the Pacific Northwest region of North America. *Journal of the American Water Resources Association*, *50*(6), 1461–1476. https://doi.org/10.1111/jawr.12199

Warner, M. D., & Mass, C. F. (2017). Changes in the climatology, structure, and seasonality of Northeast Pacific atmospheric rivers in CMIP5 climate simulations. *Journal of Hydrometeorology*, *18*(8), 2131–2141. https://doi.org/10.1175/JHM-D-16-0200.1

Warner, M. D., Mass, C. F., & Salathé, E. P. Jr. (2015). Changes in winter atmospheric rivers along the North American west coast in CMIP5 climate models. *Journal of Hydrometeorology*, *16*(1), 118–128. https://doi.org/10.1175/JHM-D-14-0080.1

Water Survey of Canada (2016). HYDAT Database, National Water Data Archive. Retrieved from http://www.ec.gc.ca/rhc-wsc/default.asp?lang=En&n=9018B5EC-1/, last access 15 September, 2016.

Werner, A. T., & Cannon, A. J. (2016). Hydrologic extremes—An intercomparison of multiple gridded statistical downscaling methods. *Hydrology and Earth System Sciences*, *20*(4), 1483–1508. https://doi.org/10.5194/hess-20-1483-2016.

Whitfield, P. H., Cannon, A. J., & Reynolds, C. J. (2002). Modelling streamflow in present and future climates: Examples from the Georgia Basin, British Columbia. *Canadian Water Resources Journal*, *27*(4), 427–456. https://doi.org/10.4296/cwrj2704427

Whitfield, P. H., Wang, J. Y., & Cannon, A. J. (2003). Modelling future streamflow extremes—Floods and low flows in Georgia basin, British Columbia. *Canadian Water Resources Journal*, *28*(4), 633–656. https://doi.org/10.4296/cwrj2804633